



HAL
open science

Fashioning Prussian Blue Nanoparticles by Adsorption of Luminophores: Synthesis, Properties, and in Vitro Imaging

Ekaterina Mamontova, Morgane Daurat, Jérôme Long, Anastasia Godefroy, Fabrice Salles, Yannick Guari, Magali Gary-Bobo, Joulia Larionova

► **To cite this version:**

Ekaterina Mamontova, Morgane Daurat, Jérôme Long, Anastasia Godefroy, Fabrice Salles, et al.. Fashioning Prussian Blue Nanoparticles by Adsorption of Luminophores: Synthesis, Properties, and in Vitro Imaging. *Inorganic Chemistry*, 2020, 59 (7), pp.4567-4575. 10.1021/acs.inorgchem.9b03699 . hal-02538711

HAL Id: hal-02538711

<https://hal.science/hal-02538711>

Submitted on 18 Nov 2020

HAL is a multi-disciplinary open access archive for the deposit and dissemination of scientific research documents, whether they are published or not. The documents may come from teaching and research institutions in France or abroad, or from public or private research centers.

L'archive ouverte pluridisciplinaire **HAL**, est destinée au dépôt et à la diffusion de documents scientifiques de niveau recherche, publiés ou non, émanant des établissements d'enseignement et de recherche français ou étrangers, des laboratoires publics ou privés.

Fashioning Prussian blue nanoparticles by adsorption of luminophores: synthesis, properties and *in vitro* imaging

*Ekaterina Mamontova,^{a, ‡} Morgane Daurat,^{b,c, ‡} Jérôme Long,^{*a} Anastasia Godefroy,^{b,c} Fabrice Salles,^d Yannick Guari,^a Magali Gary-Bobo^{*b} and Joulia Larionova^a.*

a. Institut Charles Gerhardt, UMR 5253, Equipe Ingénierie Moléculaire et Nano-Objets, Université de Montpellier, ENSCM, CNRS. Place Eugène Bataillon, 34095 Montpellier Cedex 5, France, E-mail : jerome.long@umontpellier.fr

b. Institut des Biomolécules Max Mousseron, UMR5247, Université de Montpellier, CNRS, ENSCM, Faculté de Pharmacie, 15 Avenue Charles Flahault, 34093 Montpellier Cedex 05, France. E-mail : magali.gary-bobo@inserm.fr

c. NanoMedSyn, 15 Avenue Charles Flahault, 34093 Montpellier Cedex 5, France

d. Institut Charles Gerhardt Montpellier, UMR 5253, Equipe Agrégats, Interfaces et Matériaux pour l'Energie ENSCM/CNRS/UM, Place Eugène Bataillon, 34095 Montpellier Cedex 5, France.

We report the post-synthetic functionalization of Prussian blue (PB) nanoparticles by two different luminophores (2-aminoanthracene and rhodamine B). We show that the photoluminescence properties of the fluorophores are modified by a confinement effect upon adsorption and demonstrate that such multifunctional nanosized systems could be used for in vitro imaging.

Introduction

Prussian blue (PB) and their analogues are widely recognized as the first coordination network materials in which transition metal ions are assembled through cyano-bridges, generating a 3D cubic structure. PB is a mixed-valence system exhibiting the general formula $A_{1-x}Fe^{III}[Fe^{II}(CN)_6]_{1-x/4}\square_{x/4}$, in which A is an alkaline ion and \square denotes the hexacyanoferrate vacancies. The synthesis of PB at the nanoscale has recently attracted a great deal of interest due to several advantages arising from their molecule-based nature with respect to classical inorganic nanoparticles.¹ More specifically, an upturn has recently been taken to utilize PB nanoparticles for biomedical applications thanks to their adjustable physical and chemical properties, their porosity and their chemical robustness in water over a large pH range.² Moreover, they benefit from an excellent biocompatibility since the so-called “insoluble” form of the bulk PB has been approved by the Food and Drug Administration (FDA) as an antidote for radioactive Cs^+ and nonradioactive Tl^+ poisoning.³ Consequently, the efficiency of nanosized PB has been demonstrated for a myriad of biomedical applications including Magnetic Resonance Imaging (MRI),⁴ scintigraphy,⁵ photoacoustic imaging,⁶ or therapy through different kinds of treatment⁷ together with drug delivery^{7a},⁸ and photothermal therapy.⁹

On the other hand, fluorescence imaging is an affordable technique that benefits from a high temporal resolution and high sensitivity.¹⁰ Numerous nanosized systems, such as gold and lanthanide-based upconverting nanoparticles or semiconductors quantum dots have been

employed for optical imaging.¹¹ This approach has recently been extended to nanosized Metal-Organic Framework.¹² In this sense, optical imaging would be therefore highly needed to fully exploit the potentials of nanosized PB with the aim to easily monitor the nanoparticles uptake into the cells, understand their biodistribution and the efficiency of the targeted treatment. However, efforts to implement luminescence in these intrinsically multifunctional PB nanosystems remain almost unexplored except the two examples of Mn²⁺-doped PB nanoparticles with an avidin functionalized surface and core@shell polypyrrole@PB nanoparticles.^{4e, 13} Combining the aforementioned properties of nanosized PB with luminescence would therefore allow the design of simple theranostic agents.¹⁴ Hence, new luminescent PB nanoparticles with different emission ranges are therefore required.

In this sense, various synthetic approaches could be used to post-functionalize PB nanoparticles. Firstly, surface modification of the PB nanoparticles could be achieved using bulky ligands able to interact with the metal ions located at the surface.¹⁵ On the other hand, we have also recently reported an original strategy to render magnetic nickel hexacyanochromate nanoparticles luminescent by a post-synthetic functionalization within the internal porosity of the cyano-bridged framework using the 2-aminoanthracene (AA) fluorophore to yield a bifunctional magneto-luminescent system.¹⁶ Taking advantage of these simple methodologies, we have extended this to PB nanosystems by their functionalization with two different fluorophores. We report here the understanding of PB nanoparticles' functionalization by combining experimental and theoretical methods as well as the in-depth investigation of their photophysical properties and cellular uptake.

Experimental Section

Materials and Methods

All chemical reagents were purchased and used without further purification: Iron (III) chloride hexahydrate (Sigma Aldrich, 97%), Sodium hexacyanoferrate (II) decahydrate (Alfa Aesar, 99%), 2-aminoanthracene (Alfa Aesar, 94%), Rhodamine B (Acros Organics, 98+%), ultra-pure water, ethanol 96% vol (TechniSolv), SnakeSkin Dialysis Tubing (3,5000 MWCO, 22 mm × 35 feet dry diameter, 34 mm dry flat width, ThermoScientific).

Synthesis of Na⁺/Fe³⁺/[Fe^{II}(CN)₆]⁴⁻ PB nanoparticles (1).

The PB nanoparticles (NPs) were obtained following general procedures.^{9c, 17} At 25°C, aqueous solutions of FeCl₃·6H₂O (10.00 mM, 10 mL) and Na₄[Fe(CN)₆]·10H₂O (11.25 mM, 10 mL) were added simultaneously to 100 mL of pure water at 2 mL·h⁻¹ rate, using a syringe pump. After addition, the mixture was stirred one hour before being centrifuged at 37,500 × g (20,000 rpm) during 15 min. The supernatant was removed and the NPs were washed successively with water and ethanol and dried under vacuum to obtain a dark blue powder.

IR (KBr): ν(O-H) = 3630 cm⁻¹ (coordinated water), ν(O-H) = 3400 cm⁻¹ (crystallized water), ν(C≡N) = 2082 cm⁻¹ (Fe^{III}-C≡N-Fe^{II}), δ(O-H) = 1606 cm⁻¹ (crystallized water), ν(Fe^{II}-CN) = 602 cm⁻¹, δ(Fe^{II}-CN) = 501 cm⁻¹.

EDS: 14.04/85.96 (Na/Fe). Formula found: Na_{0.30}Fe^{III}[Fe^{II}(CN)₆]_{0.82}·3.7H₂O.

Elemental analysis calcd (%): C, 19.49; H, 2.44; N, 22.72; found (%): C, 19.22; H, 3.36; N, 22.15.

Post-synthetic functionalization of Na⁺/Fe³⁺/[Fe^{II}(CN)₆]⁴⁻ nanoparticles with 2-aminoanthracene (1@AA).

The post-functionalization was performed by mixing the pristine Na⁺/Fe³⁺/[Fe^{II}(CN)₆]⁴⁻ NPs **1** (30 mg, 0.10 mmol) with the 2-aminoanthracene (**AA**) (96 mg, 0.50 mmol) in ethanol for 24 h under

stirring. Then, the solution was centrifuged at $37,500 \times g$ (20,000 rpm) during 15 min. The supernatant was removed and the NPs were washed with ethanol several times. The NPs were dispersed in the minimum of ethanol to perform a 2-days dialysis using SnakeSkin Dialysis Tubing. Finally, the solid was recovered by centrifugation at $37,500 \times g$ (20,000 rpm) during 15 min and dried under vacuum to obtain a blue solid.

IR (KBr): $\nu(\text{O-H}) = 3630 \text{ cm}^{-1}$ (coordinated water), $\nu(\text{O-H}) = 3390 \text{ cm}^{-1}$ (crystallized water/primary alcohol groups), $\nu(\text{C}\equiv\text{N}) = 2078 \text{ cm}^{-1}$ ($\text{Fe}^{\text{III}}\text{-C}\equiv\text{N-Fe}^{\text{II}}$), $\nu(\text{N-H}) = 1635 \text{ cm}^{-1}$ (N-H amine), $\delta(\text{O-H}) = 1609 \text{ cm}^{-1}$ (crystallized water), $\nu(\text{C-C}) = 1485\text{-}1410 \text{ cm}^{-1}$ (aromatic), $\nu(\text{C-H}) = 1346\text{-}600 \text{ cm}^{-1}$ (aromatic), $\nu(\text{Fe}^{\text{II}}\text{-CN}) = 600 \text{ cm}^{-1}$, $\delta(\text{Fe}^{\text{II}}\text{-CN}) = 501 \text{ cm}^{-1}$.

EDS: 15.12/84.88 (Na/Fe).

Elemental analysis calcd (%): C, 21.60; H, 2.49; N, 21.05. Found (%): C, 21.33; H, 2.56; N, 20.78.

Estimated formula for **1@AA**: $\text{Na}_{0.30}\text{Fe}^{\text{III}}[\text{Fe}^{\text{II}}(\text{CN})_6]_{0.83}@\text{(AA)}_{0.08} \cdot 3.6\text{H}_2\text{O}$.

Post-synthetic functionalization of $\text{Na}^+/\text{Fe}^{3+}/[\text{Fe}^{\text{II}}(\text{CN})_6]^{4-}$ nanoparticles with Rhodamine B (1@RhB**).**

The post-functionalization was performed by mixing the pristine $\text{Na}^+/\text{Fe}^{3+}/[\text{Fe}^{\text{II}}(\text{CN})_6]^{4-}$ NPs **1** (30 mg, 0.1 mmol) with the rhodamine B (**RhB**) (240 mg, 0.50 mmol) in ultrapure water for 24 h under stirring. Then, the solution was centrifuged at $37,500 \times g$ (20,000 rpm) during 15 min. The supernatant was removed and the NPs were washed with water several times. The NPs were dispersed in the minimum of water to perform a 2-days dialysis using SnakeSkin Dialysis Tubing. Finally, the solid was recovered by centrifugation at $37,500 \times g$ (20,000 rpm) during 15 min, washed with water and ethanol and dried under vacuum to give a blue solid.

IR (KBr): $\nu(\text{O-H}) = 3630 \text{ cm}^{-1}$ (coordinated water), $\nu(\text{O-H}) = 3400 \text{ cm}^{-1}$ (crystallized water/primary alcohol groups), $\nu(\text{C}\equiv\text{N}) = 2082 \text{ cm}^{-1}$ ($\text{Fe}^{\text{III}}\text{-C}\equiv\text{N-Fe}^{\text{II}}$), $\nu(\text{C=O}) = 1691 \text{ cm}^{-1}$ (COOH acide), $\nu(\text{C=N}) = 1635 \text{ cm}^{-1}$, $\delta(\text{O-H}) = 1606 \text{ cm}^{-1}$ (crystallized water), $\nu(\text{C-C}) = 1485\text{-}1410 \text{ cm}^{-1}$ (aromatic), $\nu(\text{C-H}) = 1346\text{-}600 \text{ cm}^{-1}$ (aromatic), $\nu(\text{Fe}^{\text{II}}\text{-CN}) = 603 \text{ cm}^{-1}$, $\delta(\text{Fe}^{\text{II}}\text{-CN}) = 501 \text{ cm}^{-1}$.

EDS: 11.59/88.06 (Na/Fe).

Elemental analysis calcd (%): C, 18.29; H, 2.53; N, 20.45. Found (%): C, 18.57; H, 2.62; N, 20.95.

Estimated formula for **1@RhB**: $\text{Na}_{0.23}\text{Fe}^{\text{III}}[\text{Fe}^{\text{II}}(\text{CN})_6]_{0.81}@\text{(RhB)}_{0.02}\cdot 3.7\text{H}_2\text{O}$.

Luminophore's release

In order to estimate the possibility of luminophores' leaching, the NPs **1@AA** or **1@RhB** (10 mg) were dispersed in 3 mL of ultrapure water to perform a 24-hours dialysis using SnakeSkin Dialysis tubing in 10 mL of water. The NPs were removed by centrifugation and the receiving medium was studied by UV-Vis spectroscopy.

Cell culture

Human breast adenocarcinoma MDA-MB-231-GFP and MDA-MB-231 cell lines were used. MDA-MB-231 cell line stably expresses GFP inducing the visualization of green nuclei in contrast to MDA-MB-231. Cells were cultured in Dulbecco's Modified Eagle's Medium (DMEM) supplemented with 10% fetal bovine serum and antibiotic (0.05 mg.mL⁻¹ gentamicin). These cells grown in humidified atmosphere at 37°C and under 5% CO₂.

Cytotoxicity experiments

MDA-MB-231 cells were seeded in 96-well plates. After 24 h of cell growth, cells were treated with increasing concentrations (0, 50, 100, 150 and 200 $\mu\text{g.mL}^{-1}$) of nanoparticles (**1**, **1@AA** and **1@RhB**). Three days after treatment, cells were stained with nuclei colorant (Hoechst) and visualized with microscope. The cells were counted using ImageJ program.

Infrared Spectroscopy

Infrared spectra were recorded as KBr disks on a PerkinElmer Spectrum two spectrophotometer.

Ultraviolet-visible spectroscopy

UV-Vis spectra were collected on a JASCO V-650 spectrometer in water or ethanol ($C = 500 \mu\text{g.mL}^{-1}$).

X-ray Powder Diffraction

X-ray powder diffraction patterns were recorded in the 2θ interval $5-60^\circ$ at room temperature with the PANalytical X'Pert Powder diffractometer analytical diffractometer mounted in a Debye-Scherrer configuration and equipped with Cu radiation ($\lambda = 1.5418 \text{ \AA}$).

Thermogravimetric Analysis

Thermogravimetric analyses were obtained with a thermal analyser STA 409 Luxx® (Netzsch) in the range $25 - 650 \text{ }^\circ\text{C}$ at heating speed of $5 \text{ }^\circ\text{C.min}^{-1}$.

Zeta potential measurements

Zeta potential measurements were performed with a Zetasizer Nano-series Malvern instrument. Aqueous suspension were used ($C = 1 \text{ mg.mL}^{-1}$). Three individual measurements were accumulated and averaged until the final zeta potential result was achieved.

Electron microscopy

Transmission Electron Microscopy (TEM) observations were carried out at 100 kV (JEOL 1200 EXII). Samples for TEM measurements were deposited from solutions on copper grids. Nanoparticles' size distribution histograms were determined using enlarged TEM micrographs taken at magnification of 100 K on a statistical sample of *ca.* 300 nanoparticles.

TEM imaging

MDA-MB-231 cells were seeded on glass coverslips for 24 h. After controlling their adherence and growing, cells were exposed (or not for Control tests) to $100 \text{ } \mu\text{g. mL}^{-1}$ of **1@AA** and **1@RhB** for 20 h. The medium was removed and cells were washed twice with DPBS. Cells were fixed by incubation with 2.5% (v/v) glutaraldehyde in DPBS buffer and stored at 4°C. Then, cells were extensively washed with DPBS. The staining of samples was obtained upon incubation with 1% osmium tetroxide. Samples were dehydrated by ascending grades of EtOH; for impregnation, the samples were firstly treated with a mix EtOH/EPON resin (1:1, v/v) for 1 h, and twice in EPON for 2 h. The polymerization was performed by embedding cells in EPON resin for 12 h at 60°C, plunged in liquid nitrogen at -195°C to detach the coverslip, and placed for two days at 60°C for completing polymerization. The ultrathin sections (70 nm) were obtained using an ultramicrotome (Leica Ultracut) and disposed on the copper grids. The grids were incubated in uranyl acetate for 2 min, rinsed in water, and then incubated in lead citrate for 2 min, and finally rinsed with water.

Scanning Electronic Microscopy

Scanning Electronic Microscopy (EDS) analyses were performed on a FEI Quanta FEG 200 instrument. The powders were deposited on an adhesive carbon film and analyzed under vacuum. The quantification of the heavy elements was carried out with the INCA software, with a dwell time of 3 μ s.

Photoluminescence measurements

The emission and excitation spectra were recorded at 295 K using an Edinburgh FLS-920 spectrofluorimeter in water or ethanol suspension ($C = 500 \mu\text{g.mL}^{-1}$) or for powdered samples. The excitation source was a 450 W Xe arc lamp. The emission spectra were corrected for detection and optical spectral response of the spectrofluorometer.

Photostability

Ethanolic suspensions ($500 \mu\text{g.mL}^{-1}$) were irradiated in a Edinburgh FLS-920 spectrofluorimeter (maximum slits opening) during 16 hours at 365 and 520 nm for **1@AA** and **1@RhB** respectively.

Cellular uptake

The cellular uptake experiment was performed using confocal fluorescence microscopy on living cells. MDA-MB-231-GFP cells were plated onto bottom glass dishes (World Precision Instrument, Stevenage, UK) in 1 mL culture medium for 24 h. Cancerous cells were treated or not for 20 h with **1@AA** or **1@RhB** at a concentration of $100 \mu\text{g.mL}^{-1}$, and **AA** or **RhB** at the same grafted concentration on **1**. Before the visualization, cells were washed two times with culture medium. Confocal fluorescence microscopy observations were carried out at Carl Zeiss Microscope. The

measurements were performed on living cells under a 488 nm wavelength excitation for nucleus, 458 nm for **AA** and 561 nm for **RhB**. All images were performed with a high magnification (63x/1.4 OIL DIC Plan-Apo).

Conventionally, GFP signal was represented in green, here GFP is in blue in order to show the **AA** fluorescence in green. In addition, MDA-MB-31-GFP cells were used for confocal imaging to have nuclei labeling other than DAPI, in order to avoid the excitation spectrum overlap between DAPI and **AA**.

Internalization quantification by FACS

MDA-MB-231 cells were treated or not with $100 \mu\text{g}\cdot\text{mL}^{-1}$ of **1@RhB** for 1, 3, 6 and 24 h. After treatment, control and treated cells were washed once in cold Phosphate Buffer Saline (PBS), harvested and centrifuged (1300 rpm, 5 min). Cell pellet were resuspended in PBS enriched with CaCl_2 , MgCl_2 and stained by propidium iodide ($1 \mu\text{g}\cdot\text{mL}^{-1}$) (Sigma-Aldrich Chimie, Lyon, France), a cell death indicator. Flow cytometric determination of living cells and micelles with FITC positive cells was done by FACS CytoFlex Flow Cytometer (Beckman Coulter, France) with a minimum of 10.000 living cells collected.

Computational section

Monte Carlo simulations were performed at 300 K to determine the amount adsorbed at saturation for both, **RhB** and **AA** in the PB structure **1**, as well as the adsorption energy between the first adsorbed molecule and the PB framework. During these simulations, 3D periodic boundary conditions were applied, while the **AA** and **RhB** molecules can undergo different motions including translation, rotation, deletion and insertion randomly considered during the equilibration

steps. In order to predict the amount adsorbed in a porosity, a standard methodology based on the equilibrium of chemical potentials between the adsorbed phase inside the pores and the pseudo gaseous phase at a given temperature was considered. For that purpose, 5×10^6 steps for equilibration and 5×10^6 steps of production were considered for calculations using Universal Force Field (UFF) combined with partial charges for both the molecules and the framework. The force fields were implemented in the home-made Monte Carlo code. Following the strategy proposed in Rojas et al.,¹⁸ ESP charges were extracted from DMol3 calculations for **RhB** and **AA** molecules, while qEq partial charges (corresponding to the partial charges obtained from the electronegativity equalization method) were considered for the solid framework and formal charges for the compensating cations. Concerning the Lennard Jones interactions, the Lorentz-Berthelot rules were applied with a cut-off radius fixed at 12.5 Å. Ewald summation for the electrostatic part was handled to increase the convergence for the energy calculations.

The structures considered for the solid have already been presented in the literature and reproduced in Scheme 1.

From these Monte Carlo calculations, it is therefore possible to determine the ability of the internal porosity of the solid to accommodate both AA and RhB molecules. Indeed different positions of the molecules are tested during the simulations with a large number of equilibration steps.

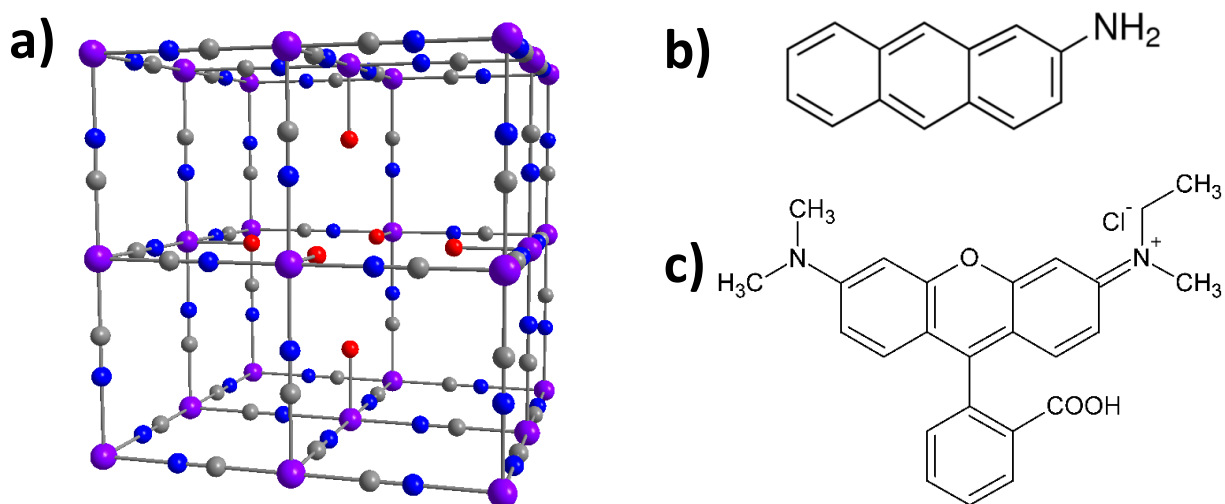
In addition, classical calculations performed with GULP have been used to optimize the geometry of the solid considering a chemical interaction with the **AA** in order to compare the physical interaction (similar to adsorption of the molecule) and the chemical interaction (similar to chemisorption of the molecule on the unsaturated metal center). For these calculations, the same parameters used before have been considered.

The molecular simulations have focused on the microscopic pores and not on the mesopores, which were present in the structure. From Monte Carlo simulations, the adsorption enthalpy at low coverage (1 molecule per cell unit) is estimated at $-30 \text{ kcal.mol}^{-1}$, which is weaker than the chemical interaction between **AA** and **1** (evaluated at $-120 \text{ kcal.mol}^{-1}$) calculated using similar force fields. This value is obtained from the difference between the energy of the {PB + AA} structure (where the **AA** is interacting with the Fe^{3+} cation by NH_2 group) and the sum of the energy of the empty PB structure and the energy of the **AA** molecule. These results point out that **AA** should interact with **1** by strong chemical coordination interactions.

In complement, the pore size distribution has been calculated using the same parametrization for the framework (UFF) and the methodology developed by Gelb and Gubbins, considering a probe sphere including in the porosity and for which the diameter is growing up to contact of the solid surface.¹⁹ The pores size distribution shows two different types: the tetrahedral sites of the *fcc* structure (with pore diameter close to 4 Å) and larger pores (with pore radius estimated at 7.5 Å from Figure S9 if we consider a spherical ball to probe the porosity, ~~but the pores are elongated and dimensions are close to 7.5 Å x 7.5 Å x 20 Å~~) formed by cyanometallates vacancies. Due to the shape of these pores (cubic and elongated for mono-lacuna and bi-lacuna containing PB models respectively), they are suitable to accommodate **AA** of 10 Å x 5 Å x 1 Å, but are unable to accommodate **RhB** of 16 x 12 x 7 Å. Indeed mono-lacunae generated by single cyanometallate vacancies have a diameter that can be estimated at 7.5 Å x 7.5 Å x 11 Å, while bi-lacuna generated by double cyanometallate vacancies have a diameter estimated at 7.5 Å x 7.5 Å x 20 Å. Keep in mind that these two kinds of pores cannot be distinguished by the probe sphere approach since the lowest dimension imposes the diameter of the sphere.

Results and discussion

Synthesis and characterizations. Implementing luminescence in our PB nanosized systems was performed by a two-steps procedure involving the synthesis of surfactant-free PB nanoparticles, followed by their post-functionalization with two targeted luminophores, 2-aminoanthracene (**AA**) and Rhodamine B (**RhB**), which differ from their size and emission features (Scheme 1). They were selected since: (i) they present different colour of emission (green for **AA** and red for **RhB**) under excitation in different domains (300 – 450 for **AA** and 500 – 600 nm for **RhB**) interesting for biomedical imaging;²⁰ (ii) both of them are planar, but present different sizes in comparison to the PB's porosity generated by the double vacancies; (iii) they present different functions able or not to form chemical bonds with PB network. In contrast to **AA**, the large size of **RhB** most likely prevents its adsorption within the porosity, but the surface functionalization may be achieved either by electrostatic (ammonium interacting with negatively charged PB nanoparticles) or covalent (carboxylic moieties) interactions as observed with in citrate stabilized PB nanoparticles.^{4i, 4j}



Scheme 1. a) Typical structure of a lacunary PB. Color code: purple, Fe^{II} and Fe^{III}., blue, N; grey, C; red, O. b) Chemical structure of **AA**. c) Chemical structure of **RhB**.

Surfactant free PB nanoparticles $\text{Na}_{0.30}\text{Fe}^{\text{III}}[\text{Fe}^{\text{II}}(\text{CN})_6]_{0.82} \cdot 3.7\text{H}_2\text{O}$ (**1**) of 72 ± 6 nm (Figure S1) were obtained using our previously reported method of the controlled addition of the molecular precursors $\text{Na}_4[\text{Fe}(\text{CN})_6] \cdot 10\text{H}_2\text{O}$ and $\text{FeCl}_3 \cdot 6\text{H}_2\text{O}$ in aqueous solution.^{9c, 17} **1** was subsequently re-dispersed in either ethanol or water with **AA** or **RhB**, respectively, and the mixture was reacted for 24H before being thoroughly washed and next dialyzed to fully remove any residual luminophores. Elemental and Thermogravimetric (TGA) analyses (Figure S2-S3) on the obtained solids allow estimating the water and luminophores content to give $\text{Na}_{0.30}\text{Fe}^{\text{III}}[\text{Fe}^{\text{II}}(\text{CN})_6]_{0.83} @ (\text{AA})_{0.08} \cdot 3.6\text{H}_2\text{O}$ (**1@AA**) and $\text{Na}_{0.23}\text{Fe}^{\text{III}}[\text{Fe}^{\text{II}}(\text{CN})_6]_{0.81} @ (\text{RhB})_{0.02} \cdot 3.7\text{H}_2\text{O}$ (**1@RhB**). The loading capacity, defined as the luminophore's weight divided by the total weight of the nanoparticles, is of 4.8 and 2.9 % for **1@AA** and **1@RhB**, respectively. Besides, TGA analyses indicate that, in both cases, the luminophore's decomposition occurs at higher (**1@AA**) or similar temperatures (**1@RhB**) compared to PB. This suggests the integration of **AA** within the porosity of the PB network, while **RhB** is localized at the surface. In comparison with the pristine nanoparticles, **1@AA** and **1@RhB** exhibit similar structural features, such as a stretching cyanide $\nu(\text{Fe}^{\text{II}}\text{-CN-Fe}^{\text{III}})$ vibration located at around 2080 cm^{-1} in the FT-IR spectra (Figure S4-S5), and a Powder X-Ray Diffraction Patterns showing the typical *fcc* structure with a lattice parameter $a = 10.0 \text{ \AA}$ (Figure S6, Table S1). The post-functionalization with the luminophores is confirmed by the typical vibrations of either **AA** and **RhB** in the $600\text{-}1700 \text{ cm}^{-1}$ region (Figure S5). Scherrer analysis does not reveal a modification in the crystallite sizes with respect to the pristine nanoparticles **1** (*i.e.* 55 nm, Table S1), which is in good accordance with the Transmission Electronic Microscopy (TEM) analyses showing cubic nanoparticles with a size of 72 ± 5 nm and 73 ± 5 nm for **1@AA** and **1@RhB**, respectively (Figure 1, Figure S7-S8). The negative values of the zeta potentials for **1** and **1@AA** are rather similar

indicating a comparable surface state (Table S2). In contrast, a significant increase of the zeta potential is observed for **1@RhB**, while no chloride ion (that may originate from **RhB**) could be detected by the EDS analysis. All these results suggest that **AA** may be adsorbed within the porosity of the PB, whereas **RhB** cannot enter inside the internal porosity (even by considering bi-lacuna containing structure for PB) as confirmed by Monte Carlo simulations and interacts by coordination and/or electrostatically with the negatively charged surface of the PB nanoparticles. Trancher electrostatic ?

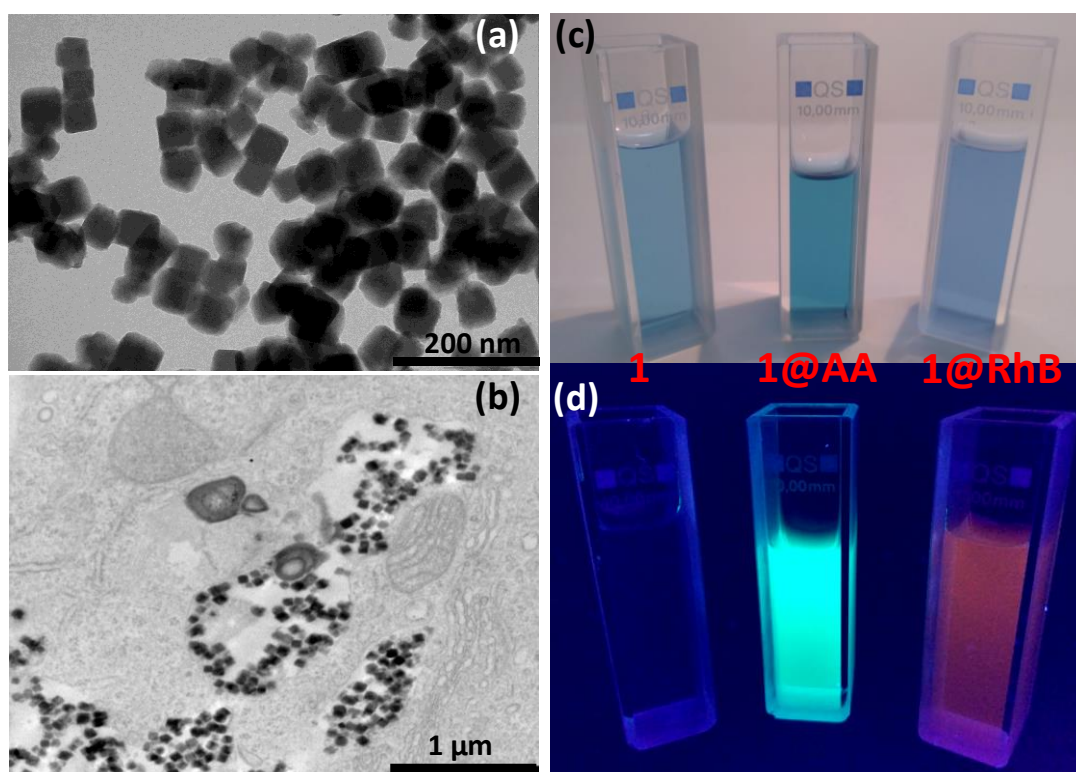


Figure 1. TEM images of **1@AA** (a) and **1@AA** in MDA-MB-231 cancer cells (b); Photographs of **1**, **1@AA** and **1@RhB** in water without excitation (c) and under excitation with an UV lamp at 365 nm showing their luminescence (d).

Molecular Simulations. To validate such assumptions, molecular simulations (Monte Carlo and classical force field-based calculations) were performed. The pores size distribution of **1** (Figure

S9) highlights two distinct porosity in the coordination network, namely the tetrahedral sites of the *fcc* structure and the larger pores of pore diameter estimated by molecular simulations at 7.5 Å but, due to the cubic shape where larger size can be calculated by considering the cube diagonale 7.5 Å × 7.5 Å × 11 Å for mono-lacuna and 7.5 Å × 7.5 Å × 20 Å for bi-lacuna models. These larger pores are generated by cyanometallate vacancies and suitable to accommodate only **AA** (10 Å × 5 Å × 1 Å). In contrast, the size of **RhB** (16 Å × 12 Å × 7 Å) is clearly too large to enter into these cavities, suggesting rather an interaction at the nanoparticles' surface by electrostatic or covalent bonds. Additionally, the **AA** adsorbed amount in an empty structure is estimated by Monte Carlo simulations at 0.13 **AA** molecules per unit cell (as defined below), which is slightly higher than the experimental value of 0.08. This loading capacity of 7.6 wt% is to be compared with the experimental one of 4.8 wt%. This discrepancy could be rationalized by the presence of solvent molecules, which are able to chemically interact with unsaturated metal centers (CUS) and enter in competition with **AA**. To go further, the distribution of **AA** in the pores reveals that it is adsorbed within the largest pores generated by cyanometallate vacancies (Figure 2). Complementary calculations have also been performed to quantify the interaction energy when the **AA** adsorption is mainly governed by physisorption (since Universal Force Field is unable to predict the formation of a covalent interaction). Firstly, the enthalpy corresponding to a physisorption at low coverage (1 molecule per cell) is estimated at -30 kcal.mol⁻¹, while the chemisorption involving a coordination bond between **AA** and Fe³⁺ gives a greater value of 120 kcal.mol⁻¹. This large energy difference suggests a favourable interaction by coordinative bond which is confirmed by the short distance of 1.96 Å between **AA** and Fe³⁺. Yet, it should be mentioned that additional interactions between NH₂ from **AA** and Fe³⁺ of 2.7-2.9 Å and between NH₂ and cyano-groups could be also observed (Figure 2).

Both experimental and theoretical approaches point out therefore a different mechanism of adsorption depending on the nature of the investigated luminophores: **AA** could be chemisorbed within the internal porosity of the PB framework due to its relatively small size whereas **RhB** interacts most likely at the nanoparticles's surface.

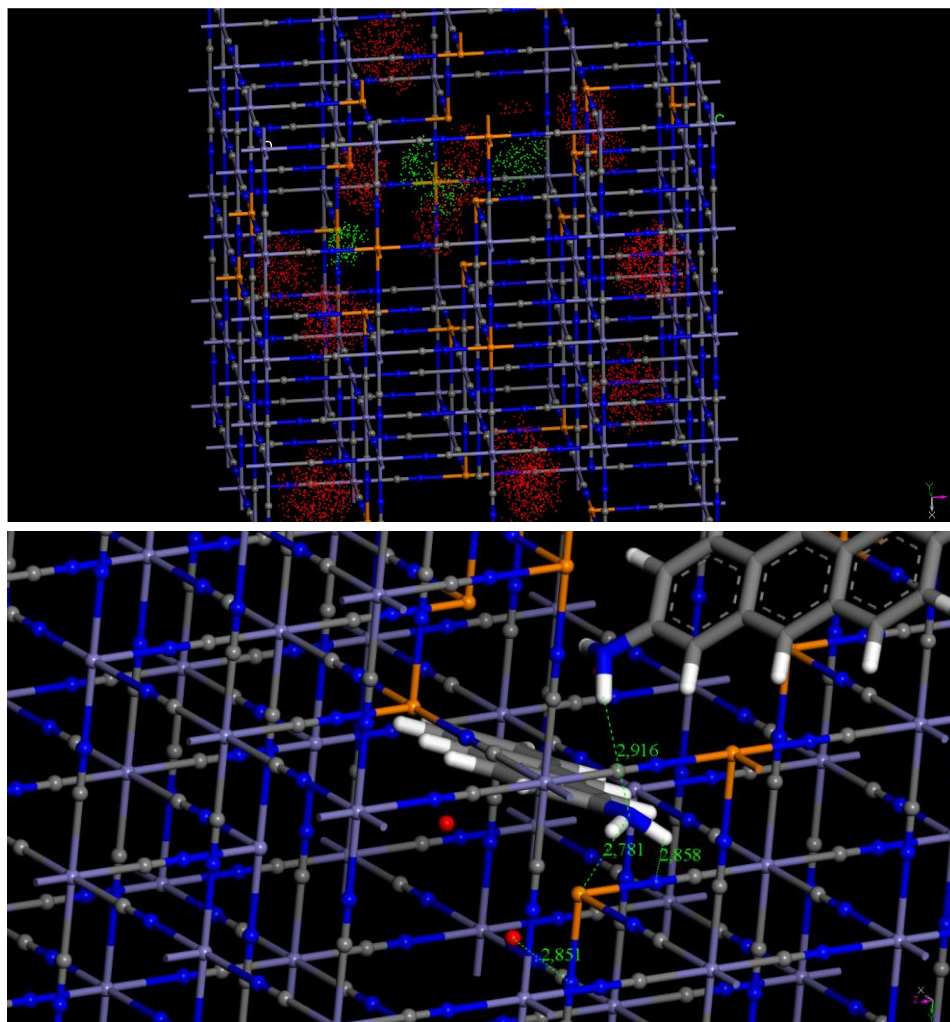


Figure 2. Top: Snapshot illustrating the density of presence of the AA molecules (green) and of the alkaline ions (red) in the empty PB structure **1** from Monte Carlo simulations. Color code for **1**: orange Fe^{3+} , light purple Fe^{2+} , blue N, grey C. Bottom: Plausible configuration of the AA molecule in PB structure **1** from Monte Carlo simulations at saturation.

Optical properties. The optical properties of the resulting functionalized PB nanoparticles were investigated in suspension and solid-state. Firstly, the electronic absorption spectra of **1@AA** and **1@RhB** show the typical broad band in the NIR associated with the intervalence $\text{Fe}^{2+}/\text{Fe}^{3+}$ charge transfer of PB (Figure 3). Moreover, the typical absorption bands related to the fluorophores could also be discerned at around 400 nm and 550 nm for **AA** and **RhB**, respectively.

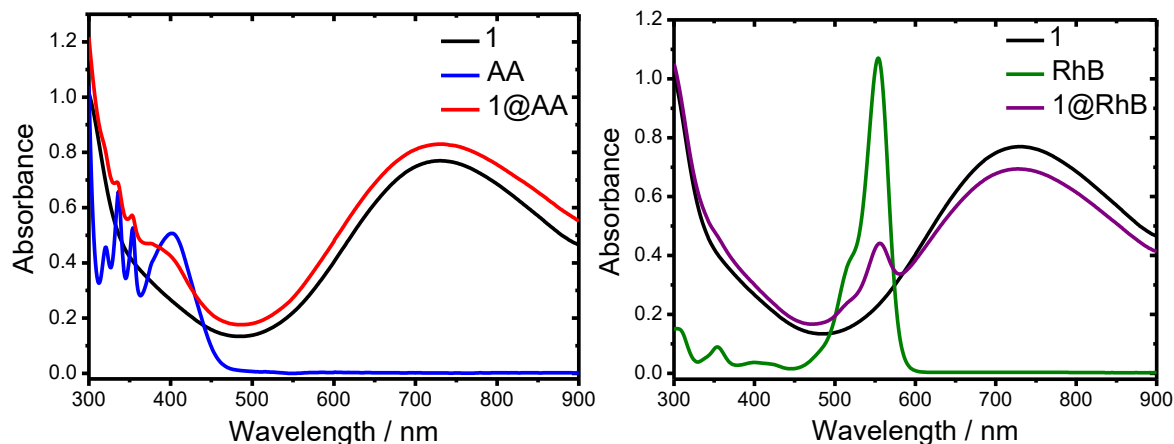


Figure 3. Left: Room temperature absorption spectra for **1**, **AA** and **1@AA** in ethanol ($500 \mu\text{g.mL}^{-1}$). Right: Room temperature absorption spectra for **1**, **RhB** and **1@RhB** in water ($500 \mu\text{g.mL}^{-1}$).

As regards the photoluminescence features, Figure 1 shows that while a suspension of **1** is optically inactive, **1@AA** and **1@RhB** exhibit a blue-green and orange emission, respectively, when excited by a UV-lamp. For both functionalized systems, the photoluminescence spectra acquired in suspension exhibit a blue-shift (*e.g.* 10 nm) with respect to the isolated luminophores (Figure 4, Figure S10). Such phenomenon has previously been observed in related functionalized PBA nanoparticles and could be ascribed to a modification of the environment of the luminophores upon adsorption.¹⁶ Thus, when excited in the UV, suspension of **1@AA** exhibits a broad emission band located at 500 nm, while the excitation of **1@RhB** at 520 nm shows an emission band centred at 575 nm (Figure 4, Figures S11-S12). In solid-state, **1@AA** displays a comparable green emission

feature at the exception of a weak emission component located in the 400-430 nm region (Figure S13) which has previously been identified as being dependent on the chromophore's concentration upon adsorption in PBA.¹⁶ In contrast, the solid-state emission spectrum for **1@RhB** (Figure S14) is comparable to that obtained in aqueous suspension, while only a red-shifted emission is observed for the **RhB** due to the well-known concentration effect (fluorophore-fluorophore interactions).²¹ Aqueous suspensions of **1**, **1@AA** and **1@RhB** are found to be stable for several hours (Figure S15).

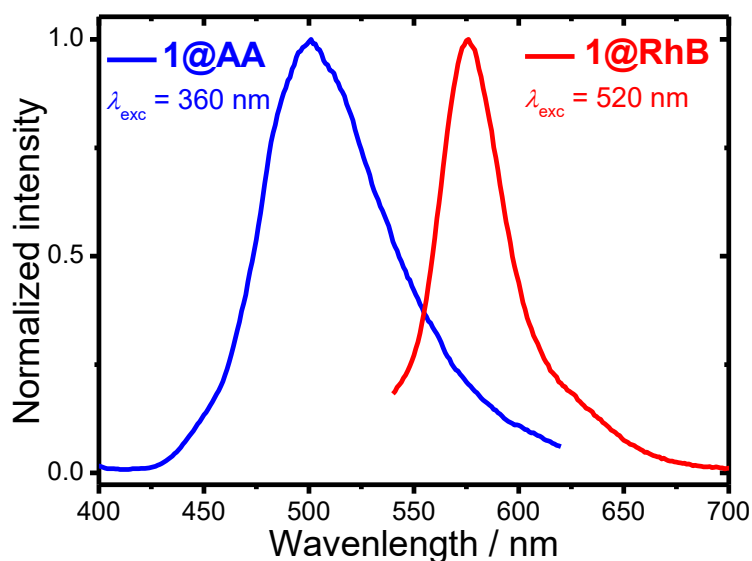


Figure 4. Room temperature normalized emission spectra for **1@AA** (excited at 360 nm) and **1@RhB** (excited at 520 nm) re-dispersed in ethanol ($500 \mu\text{g}\cdot\text{mL}^{-1}$).

Moreover, the photostability of the functionalized nanoparticles was investigated upon long-time exposure (16 H) to their respective excitation wavelengths, 365 and 520 nm for **1@AA** and **1@RhB** respectively (Figure S16). While an almost two-fold decrease (*i.e.* 48 %) in the emission intensity could be observed for **1@AA**, **1@RhB** only shows a slight reduction of less than 10 %, pointing out a remarkable photostability. Such results could be favorably compared to the free luminophores with observed decrease of 60 and 22 % for **AA** and **RbB** respectively (Figure S17).

This suggests that the luminophores are in some extent protected by their adsorption with PB nanoparticles. For both **1@AA** and **1@RhB**, no release of the luminophores could be detected after their dialysis in water during 24 h (Figure S18) confirming the strong interaction between the fluorophores and nanoparticles. These results suggest that the luminescence properties of PB nanoparticles could be used to follow *in vitro* their cell internalization.

Cellular uptake and *in vitro* imaging. Firstly, the nanoparticles safety was evaluated by studying the cytotoxicity in human breast adenocarcinoma cells (MDA-MB-231). The cells were treated with different concentrations (50, 100, 150 and 200 $\mu\text{g}\cdot\text{mL}^{-1}$) during three days. The results indicate no significant differences with the different nanoparticles at the studied doses compared to control, allowing to consider that these nanoparticles do not exhibit toxicity at these concentrations (Figure S19). Secondly, the MDA-MB-231 cells were exposed for 20 h to **1@AA** and **1@RhB** with a concentration of 100 $\mu\text{g}\cdot\text{mL}^{-1}$. Fluorescent imaging of the MDA-MB-231-GFP living cells showed that both nanoparticles were efficiently internalized by cancerous cells and after 20 h incubation are localized in cell cytoplasm (Figure 5). Comparison between **1@AA** and **1@RhB** internalization with the independent luminophores indicates that **AA** cannot be internalized by the cells in contrast to **RhB** (Figure 5, Figure S20); this later being indeed well known to cross the membranes of cells.⁴⁰ Moreover, control experiments were performed with **1** using similar conditions (Figure S21). No fluorescence could be detected demonstrating the efficiency of the post-functionalization. To ultimately confirm the cancer cell internalization of the functionalized **1@AA** and **1@RhB**, TEM imaging was performed after 20 h of incubation. The results point out a clear localization of the functionalized PB into the MDA-MB-231 cells (Figure 1, Figure S22), in accordance with the results from fluorescence imaging.

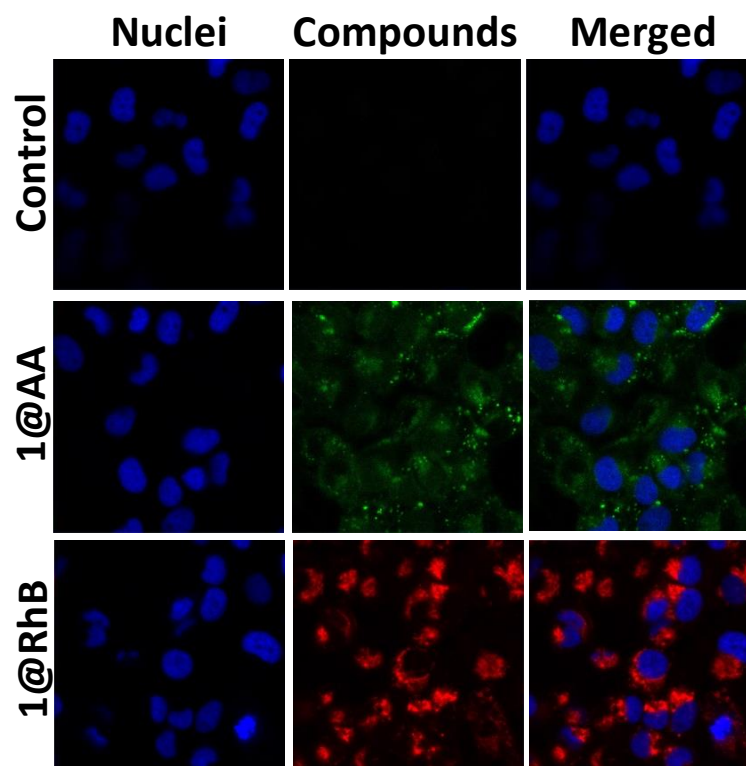


Figure 5. Human breast adenocarcinoma MDA-MB-231-GFP cells uptake of nanoparticles. Cancerous cells were incubated or not for 20 h with **1@AA** or **1@RhB** at a concentration of 100 $\mu\text{g.mL}^{-1}$. Blue emission shows the cell nucleus of MDA-MB-231-GFP cells, green and red emissions characterize the presence of **1@AA** and **1@RhB**, respectively.

Finally, quantification of the **1@RhB** internalization by cancerous cells by flow cytometry experiments was performed (Figure S23). **1@RhB** was incubated in the culture cells at a concentration of 100 $\mu\text{g.mL}^{-1}$ during different times (1 h, 3 h, 6 h and 24 h). After 3 h of incubation, a high internalization level (55% stained cells) was reached and after 24 h, 79% of cells were stained. All together, these biological experiments demonstrate the potential of such PB nanoparticles to highly penetrate the cancer cells.

Conclusions

In conclusion, we have demonstrated that PB nanoparticles could be easily post-functionalized by various luminophores to render them luminescent. Depending on the luminophore's nature, different adsorption mechanisms could be observed as confirmed by molecular modelling. With respect to the previously reported luminescent nanosized PB, the facile and low-cost character of the reported methods constitute an asset. Such approach could be easily extended to various luminophores to tune the emission range. Additionally, we unambiguously show that these simple functionalized nanosized probes could be efficiently used to monitor the cell internalization of the nanoparticles by fluorescence imaging. This opens exciting perspectives for using these PB functionalized nanoparticles for multimodal imaging.

ASSOCIATED CONTENT

Supporting Information.

Additional TEM images, TGA analyses, Infra-Red Spectra, PXRD patterns, nanoparticles size distribution, pore size distribution, additional luminescence spectra, cell viability, one-photon fluorescence imaging, values of the zeta potential and crystallographic parameters. The following files are available free of charge.

AUTHOR INFORMATION

Corresponding Author

*E-mail: jerome.long@umontpellier.fr

*E-mail: magali.gary-bobo@inserm.fr

Author Contributions

The manuscript was written through contributions of all authors. All authors have given approval to the final version of the manuscript. ‡These authors contributed equally.

ACKNOWLEDGMENT

The authors thank the University of Montpellier, CNRS and PAC of ICGM.

REFERENCES

SYNOPSIS (Word Style “SN_Synopsis_TOC”). If you are submitting your paper to a journal that requires a synopsis, see the journal’s Instructions for Authors for details.

- (1) (a) Larionova, J.; Guari, Y.; Sangregorio, C.; Guerin, C., Cyano-bridged coordination polymer nanoparticles. *New. J. Chem.* **2009**, *33* (6), 1177-1190; (b) Catala, L.; Volatron, F.; Brinzei, D.; Mallah, T., Functional Coordination Nanoparticles. *Inorg. Chem.* **2009**, *48* (8), 3360-3370; (c) Dujardin, E.; Mann, S., Morphosynthesis of Molecular Magnetic Materials. *Adv. Mater.* **2004**, *16* (13), 1125-1129; (d) Catala, L.; Mallah, T., Nanoparticles of Prussian blue analogs and related coordination polymers: From information storage to biomedical applications. *Coord. Chem. Rev.* **2017**, *346*, 32-61.
- (2) Long, J.; Guari, Y.; Guerin, C.; Larionova, J., Prussian blue type nanoparticles for biomedical applications. *Dalton Trans.* **2016**, *45* (44), 17581-17587.
- (3) (a) Nigrovic, V., Retention of Radiocaesium by the Rat as Influenced by Prussian Blue and Other Compounds. *Phys. Med. Biol.* **1965**, *10* (1), 81-92; (b) Melo, D. R.; Lipsztein, J. L.; Oliveira, C. A. N.; Bertelli, L., ¹³⁷Cs Internal Contamination Involving a Brazilian Accident, and the Efficacy of Prussian Blue Treatment. *Health Physics* **1994**, *66* (3), 245-252; (c) Pearce, J., Studies of any toxicological effects of Prussian blue compounds in mammals--a review. *Food Chem. Toxicol.* **1994**, *32* (6), 577-582; (d) Thompson, D. F.; Church, C. O., Prussian Blue for Treatment of Radiocesium Poisoning. *Pharmacotherapy* **2001**, *21* (11), 1364-1367; (e) Ruprecht, J., Problems in the supply of antidotes—A view from the pharmaceutical industry. *Toxicology* **2007**, *233* (1–3), 20-22.
- (4) (a) Cai, X.; Gao, W.; Zhang, L.; Ma, M.; Liu, T.; Du, W.; Zheng, Y.; Chen, H.; Shi, J., Enabling Prussian Blue with Tunable Localized Surface Plasmon Resonances: Simultaneously Enhanced Dual-Mode Imaging and Tumor Photothermal Therapy. *ACS Nano* **2016**, *10* (12), 11115-11126; (b) Zhu, W.; Liu, K.; Sun, X.; Wang, X.; Li, Y.; Cheng, L.; Liu, Z., Mn²⁺-Doped Prussian Blue Nanocubes for Bimodal Imaging and Photothermal Therapy with Enhanced Performance. *ACS Appl. Mater. Interfaces* **2015**, *7* (21), 11575-11582; (c) Perrier, M.; Gallud,

A.; Ayadi, A.; Kennouche, S.; Porredon, C.; Gary-Bobo, M.; Larionova, J.; Goze-Bac, C.; Zanca, M.; Garcia, M.; Basile, I.; Long, J.; de Lapuente, J.; Borrás, M.; Guari, Y., Investigation of cyano-bridged coordination nanoparticles $Gd^{3+}/[Fe(CN)_6]^{3-}/d$ -mannitol as T1-weighted MRI contrast agents. *Nanoscale* **2015**, *7* (28), 11899-11903; (d) Paul, G.; Prado, Y.; Dia, N.; Riviere, E.; Laurent, S.; Roch, M.; Elst, L. V.; Muller, R. N.; Sancey, L.; Perriat, P.; Tillement, O.; Mallah, T.; Catala, L., MnII-containing coordination nanoparticles as highly efficient T1 contrast agents for magnetic resonance imaging. *Chem. Commun.* **2014**, *50* (51), 6740-6743; (e) Dumont, M. F.; Yadavilli, S.; Sze, R. W.; Nazarian, J.; Fernandes, R., Manganese-containing Prussian blue nanoparticles for imaging of pediatric brain tumors. *Int. J. Nanomed.* **2014**, *9* (1), 2581-95; (f) Dumont, M. F.; Hoffman, H. A.; Yoon, P. R. S.; Conklin, L. S.; Saha, S. R.; Paglione, J.; Sze, R. W.; Fernandes, R., Biofunctionalized Gadolinium-Containing Prussian Blue Nanoparticles as Multimodal Molecular Imaging Agents. *Bioconjugate Chem.* **2014**, *25* (1), 129-137; (g) Perrier, M.; Kenouche, S.; Long, J.; Thangavel, K.; Larionova, J.; Goze-Bac, C.; Lascialfari, A.; Mariani, M.; Baril, N.; Guérin, C.; Donnadiéu, B.; Trifonov, A.; Guari, Y., Investigation on NMR Relaxivity of Nano-Sized Cyano-Bridged Coordination Polymers. *Inorg. Chem.* **2013**, *52* (23), 13402-13414; (h) Chelebaeva, E.; Larionova, J.; Guari, Y.; Ferreira, R. A. S.; Carlos, L. D.; Trifonov, A. A.; Kalaivani, T.; Lascialfari, A.; Guerin, C.; Molvinger, K.; Datas, L.; Maynadier, M.; Gary-Bobo, M.; Garcia, M., Nanoscale coordination polymers exhibiting luminescence properties and NMR relaxivity. *Nanoscale* **2011**, *3* (3), 1200-1210; (i) Shokouhimehr, M.; Soehnlén, E. S.; Khitrin, A.; Basu, S.; Huang, S. D., Biocompatible Prussian blue nanoparticles: Preparation, stability, cytotoxicity, and potential use as an MRI contrast agent. *Inorg. Chem. Commun.* **2010**, *13* (1), 58-61; (j) Shokouhimehr, M.; Soehnlén, E. S.; Hao, J.; Griswold, M.; Flask, C.; Fan, X.; Basilion, J. P.; Basu, S.; Huang, S. D., Dual purpose Prussian blue nanoparticles for cellular imaging and drug delivery: a new generation of T1-weighted MRI contrast and small molecule delivery agents. *J. Mater. Chem.* **2010**, *20* (25), 5251-5259; (k) Guari, Y.; Larionova, J.; Corti, M.; Lascialfari, A.; Marinone, M.; Poletti, G.; Molvinger, K.; Guerin, C., Cyano-bridged coordination polymer nanoparticles with high nuclear relaxivity: toward new contrast agents for MRI. *Dalton Trans.* **2008**, (28), 3658-3660; (l) Li, Y.; Li, C. H.; Talham, D. R., One-step synthesis of gradient gadolinium ironhexacyanoferrate nanoparticles: a new particle design easily combining MRI contrast and photothermal therapy. *Nanoscale* **2015**, *7* (12), 5209-5216; (m) Qin, Z.; Chen, B.; Huang, X.; Mao, Y.; Li, Y.; Yang, F.; Gu, N., Magnetic internal heating-induced high performance Prussian blue nanoparticle preparation and excellent catalytic activity. *Dalton Trans.* **2019**, *48* (46), 17169-17173.

(5) Perrier, M.; Busson, M.; Massasso, G.; Long, J.; Boudousq, V.; Pouget, J. P.; Peyrottes, S.; Perigaud, C.; Porredon-Guarch, C.; de Lapuente, J.; Borrás, M.; Larionova, J.; Guari, Y., ^{201}Tl -labelled Prussian blue nanoparticles as contrast agents for SPECT scintigraphy. *Nanoscale* **2014**, *6* (22), 13425-13429.

(6) (a) Jing, L.; Liang, X.; Deng, Z.; Feng, S.; Li, X.; Huang, M.; Li, C.; Dai, Z., Prussian blue coated gold nanoparticles for simultaneous photoacoustic/CT bimodal imaging and photothermal ablation of cancer. *Biomaterials* **2014**, *35* (22), 5814-5821; (b) Liang, X.; Deng, Z.; Jing, L.; Li, X.; Dai, Z.; Li, C.; Huang, M., Prussian blue nanoparticles operate as a contrast agent for enhanced photoacoustic imaging. *Chem. Commun.* **2013**, *49* (94), 11029-11031.

(7) (a) Kandanapitiye, M. S.; Wang, F. J.; Valley, B.; Gunathilake, C.; Jaroniec, M.; Huang, S. D., Selective Ion Exchange Governed by the Irving–Williams Series in $K_2Zn_3[Fe(CN)_6]_2$ Nanoparticles: Toward a Designer Prodrug for Wilson’s Disease. *Inorg. Chem.* **2015**, *54* (4), 1212-1214; (b) Lavaud, C.; Kajdan, M.; Compte, E.; Maurel, J.-C.; laikehim, j.; Bron, P.;

Oliviero, E.; Long, J.; Larionova, J.; Guari, Y., In situ synthesis of Prussian blue nanoparticles within a biocompatible reverse micellar system for in vivo Cs⁺ uptake. *New J. Chem.* **2017**, *41* (8), 2887-2890.

(8) (a) Mukherjee, S.; Rao, B. R.; Sreedhar, B.; Paik, P.; Patra, C. R., Copper Prussian blue analogue: investigation into multifunctional activities for biomedical applications. *Chem. Commun.* **2015**, *51* (34), 7325-7328; (b) Shao-Jen, W.; Chun-Sheng, C.; Lin-Chi, C., Prussian blue nanoparticles as nanocargoes for delivering DNA drugs to cancer cells. *Sci. Techno. Adv. Mater.* **2013**, *14* (4), 044405; (c) Lian, H.-Y.; Hu, M.; Liu, C.-H.; Yamauchi, Y.; Wu, K. C. W., Highly biocompatible, hollow coordination polymer nanoparticles as cisplatin carriers for efficient intracellular drug delivery. *Chem. Commun.* **2012**, *48* (42), 5151-5153; (d) Lavaud, C.; Kajdan, M.; Compte, E.; Maurel, J.-C.; Lai Kee Him, J.; Bron, P.; Oliviero, E.; Long, J.; Larionova, J.; Guari, Y., In situ synthesis of Prussian blue nanoparticles within a biocompatible reverse micellar system for in vivo Cs⁺ uptake. *New J. Chem.* **2017**, *41* (8), 2887-2890.

(9) (a) Alkilany, A. M.; Thompson, L. B.; Boulos, S. P.; Sisco, P. N.; Murphy, C. J., Gold nanorods: Their potential for photothermal therapeutics and drug delivery, tempered by the complexity of their biological interactions. *Adv. Drug Del. Rev.* **2012**, *64* (2), 190-199; (b) Shanmugam, V.; Selvakumar, S.; Yeh, C.-S., Near-infrared light-responsive nanomaterials in cancer therapeutics. *Chem. Soc. Rev.* **2014**, *43* (17), 6254-6287; (c) Ali, L. M. A.; Mathlouthi, E.; Kajdan, M.; Daurat, M.; Long, J.; Sidi-Boulenouar, R.; Cardoso, M.; Goze-Bac, C.; Amdouni, N.; Guari, Y.; Larionova, J.; Gary-Bobo, M., Multifunctional manganese-doped Prussian blue nanoparticles for two-photon Photothermal Therapy and Magnetic Resonance Imaging. *Photodiagnosis Photodyn. Ther.* **2018**, *22*, 65-69; (d) Zou, L. W., H.; He, B.; Zeng, L.; Tan, T.; Cao, H.; He, X.; Zhang, Z.; Guo, S.; Li, Y., Current Approaches of Photothermal Therapy in Treating Cancer Metastasis with Nanotherapeutics. *Theranostics* **2016**, *6* (6), 762-772; (e) Ma, Y.; Chen, H.; Hao, B.; Zhou, J.; He, G.; Miao, Z.; Xu, Y.; Gao, L.; Zhou, W.; Zha, Z., A chloroquine-loaded Prussian blue platform with controllable autophagy inhibition for enhanced photothermal therapy. *J. Mater. Chem. B* **2018**, *6* (37), 5854-5859; (f) Liu, B.; Wang, W.; Fan, J.; Long, Y.; Xiao, F.; Daniyal, M.; Tong, C.; Xie, Q.; Jian, Y.; Li, B.; Ma, X.; Wang, W., RBC membrane camouflaged prussian blue nanoparticles for gambutolin loading and combined chemo/photothermal therapy of breast cancer. *Biomaterials* **2019**, *217*, 119301; (g) Yang, R.; Hou, M.; Gao, Y.; Zhang, L.; Xu, Z.; Kang, Y.; Xue, P., Indocyanine green-modified hollow mesoporous Prussian blue nanoparticles loading doxorubicin for fluorescence-guided tri-modal combination therapy of cancer. *Nanoscale* **2019**, *11* (12), 5717-5731.

(10) Leblond, F.; Davis, S. C.; Valdés, P. A.; Pogue, B. W., Pre-clinical whole-body fluorescence imaging: Review of instruments, methods and applications. *J. Photochem. Photobiol., B* **2010**, *98* (1), 77-94.

(11) Ibarra-Ruiz, A. M.; Rodríguez Burbano, D. C.; Capobianco, J. A., Photoluminescent nanoplatforms in biomedical applications. *Advances in Physics: X* **2016**, *1* (2), 194-225.

(12) Cui, Y.; Yue, Y.; Qian, G.; Chen, B., Luminescent Functional Metal–Organic Frameworks. *Chem. Rev.* **2012**, *112* (2), 1126-1162.

(13) Ye, S.; Liu, Y.; Chen, S.; Liang, S.; McHale, R.; Ghasdian, N.; Lu, Y.; Wang, X., Photoluminescent properties of Prussian Blue (PB) nanoshells and polypyrrole (PPy)/PB core/shell nanoparticles prepared via miniemulsion (periphery) polymerization. *Chem. Commun.* **2011**, *47* (24), 6831-6833.

(14) Qin, Z.; Li, Y.; Gu, N., Progress in Applications of Prussian Blue Nanoparticles in Biomedicine. *Advanced Healthcare Materials* **2018**, *7* (20), 1800347.

- (15) (a) Yamada, M.; Arai, M.; Kurihara, M.; Sakamoto, M.; Miyake, M., Synthesis and Isolation of Cobalt Hexacyanoferrate/Chromate Metal Coordination Nanopolymers Stabilized by Alkylamino Ligand with Metal Elemental Control. *J. Am. Chem. Soc.* **2004**, *126* (31), 9482-9483; (b) Gotoh, A.; Uchida, H.; Ishizaki, M.; Satoh, T.; Kaga, S.; Okamoto, S.; Ohta, M.; Sakamoto, M.; Kawamoto, T.; Tanaka, H.; Tokumoto, M.; Hara, S.; Shiozaki, H.; Yamada, M.; Miyake, M.; Kurihara, M., Simple synthesis of three primary colour nanoparticle inks of Prussian blue and its analogues. *Nanotechnology* **2007**, *18* (34), 345609; (c) Busquets, A. M.; Novella-Xicoy, A.; Guzmán, V.; Estelrich, J., Facile Synthesis of Novel Prussian Blue–Lipid Nanocomplexes. *Molecules* **2019**, *24* (22).
- (16) Mamontova, E.; Long, J.; Ferreira, R.; Botas, A. M. P.; Salles, F.; Guari, Y.; Carlos, L. A. D.; Larionova, J., Making Prussian blue analogues nanoparticles luminescent: effect of the luminophore confinement over the properties. *Nanoscale* **2019**, *11* (15), 7097-7101.
- (17) Maurin-Pasturel, G.; Rascol, E.; Busson, M.; Sevestre, S.; Lai-Kee-Him, J.; Bron, P.; Long, J.; Chopineau, J.; Devoisselle, J.-M.; Guari, Y.; Larionova, J., 201Tl-labeled Prussian blue and Au@Prussian blue nanoprobe for SPEC-CT imaging: influence of the size, shape and coating on the biodistribution. *Inorg. Chem. Front.* **2017**, *4* (10), 1737-1741.
- (18) Rojas, S.; Colinet, I.; Cunha, D.; Hidalgo, T.; Salles, F.; Serre, C.; Guillou, N.; Horcajada, P., Toward Understanding Drug Incorporation and Delivery from Biocompatible Metal–Organic Frameworks in View of Cutaneous Administration. *ACS Omega* **2018**, *3* (3), 2994-3003.
- (19) Gelb, L. D.; Gubbins, K. E., Pore Size Distributions in Porous Glasses: A Computer Simulation Study. *Langmuir* **1999**, *15* (2), 305-308.
- (20) (a) Yao, Q.; Bermejo Gómez, A.; Su, J.; Pascanu, V.; Yun, Y.; Zheng, H.; Chen, H.; Liu, L.; Abdelhamid, H. N.; Martín-Matute, B.; Zou, X., Series of Highly Stable Isostructural Lanthanide Metal–Organic Frameworks with Expanding Pore Size and Tunable Luminescent Properties. *Chem. Mater.* **2015**, *27* (15), 5332-5339; (b) Snare, M. J.; Treloar, F. E.; Ghiggino, K. P.; Thistlethwaite, P. J., The photophysics of rhodamine B. *J. Photochem.* **1982**, *18* (4), 335-346.
- (21) Itoh, K.; Chiyokawa, Y.; Nakao, M.; Honda, K., Fluorescence quenching processes of Rhodamine B on oxide semiconductors and light-harvesting action of its dimers. *J. Am. Chem. Soc.* **1984**, *106* (6), 1620-1627.